



**Synthesis and Characterisation of BaTiO₃-based
Piezoelectric Materials for Energy Harvester
Applications**

by

**Ku Noor Dhaniah Binti Ku Muhsen
(1740112369)**

A thesis submitted in fulfillment of the requirements for the degree of
Doctor of Philosophy

**School of Microelectronic Engineering
UNIVERSITI MALAYSIA PERLIS**

2020

ACKNOWLEDGMENT

All the praises and thanks to Allah S.W.T. This thesis would not have been possible without the guidance of my supervisor and lecturers, help from friends, and support from my husband and family.

Foremost, I would like to express my sincere gratitude to my supervisor Assoc. Prof. Ir. Ts. Dr. Rozana Aina Maulat Osman for her excellent guidance, caring, patience, providing me with an excellent atmosphere for doing research and let me experience the development of BaTiO₃-based piezoelectric materials for energy harvester applications. My research would not have been possible without her motivational support. I could not have imagined having a better advisor and mentor for my PhD. study. I am also very thankful for the valuable knowledge and experience that was shared by Assoc. Prof. Ts. Dr. Mohd Sobri Idris.

Secondly, I would like to thank the technical staff and fellow lab mates who always willing to help and give the best companion while using the lab. It would have been a lonely lab without them.

Special thanks to Assoc. Prof. Dr. Shahrir Rizal Kasjoo, Dean of School of Microelectronic Engineering, UNIMAP and also Dr. Nur Syakimah Ismail, the Postgraduate Coordinator who give this opportunity to continue my study in doctorate's degree.

I would like thank to the director of Impedance Spectroscopy Laboratory at School of Applied Physics, Universiti Kebangsaan Malaysia, Assoc. Prof. Dr. Mohammad Hafizuddin Hj Jumali for providing the permission to use the Berlincourt-type d_{33} meter YE 2730A for piezoelectric constant measurements and helped interpreted the data.

In addition, I am thankful to the Ministry of Higher Education (MOHE) Malaysia for funding this project through the Fundamental Research Grant Scheme 2018 (FRGS Grant No.: FRGS/1/2018/STG07/UNIMAP/02/4).

Last but not least, I would like to thank my husband, Zuhayr Md. Ghazaly my daughter, Puteri Zahra Zuhayr and my unborn second child who always there cheering me up and stood by me through the bad and good times. These hard works was dedicated to three of them.

TABLE OF CONTENTS

	PAGE
DECLARATION OF THESIS	i
ACKNOWLEDGMENT	ii
TABLE OF CONTENTS	iii
LIST OF TABLES	vi
LIST OF FIGURES	viii
LIST OF ABBREVIATIONS	xiv
LIST OF SYMBOLS	xv
ABSTRAK	xvii
ABSTRACT	xviii
CHAPTER 1 : INTRODUCTION	1
1.1 Background	1
1.1.1 Piezoelectric Operation Concept	2
1.1.2 Figure of Merits of Piezoelectric Materials in Energy Harvesters	4
1.1.3 Polarization Direction and Mechanical Stress Axis Nomenclature	4
1.2 Problem Statements	7
1.3 Objectives	9
1.4 Scope of Study	9
1.5 Novelty of Research Findings	12
1.6 Thesis Structure	13
CHAPTER 2 : LITERATURE REVIEW	14
2.1 Introduction	14

2.2	The Subclasses of Functional Dielectrics	14
2.3	Piezoelectric Properties for Energy Harvester Applications	15
2.4	Dielectric Properties	17
2.4.1	Impedance Spectroscopy Characterisation	18
2.5	Piezoelectric Materials	21
2.5.1	Perovskite Structure	24
2.6	The Ternary Triangle Diagram of BaTiO ₃ -BaSnO ₃ -BaZrO ₃	25
2.6.1	Barium Titanate Oxide, BaTiO ₃	26
2.6.2	Barium Zirconate Oxide, BaZrO ₃	28
2.6.3	Barium Stannate Oxide, BaSnO ₃	29
2.6.4	Zr-doped BaTiO ₃ (BZT)	30
2.6.5	Sn-doped BaTiO ₃ (BST)	33
2.6.6	Sn-doped BaZrO ₃ (BSZ)	35
2.7	Sn and Zr co-doped BaTiO ₃ (BSZT)	35
2.8	Ca and Zr co-doped BaTiO ₃ (BCZT)	37
2.9	Ca and Sn co-doped BaTiO ₃ (BCST)	39
2.10	Ca, Sn and Zr triple doped BaTiO ₃ (BCSZT)	41
2.11	The Piezoelectric and Dielectric Properties of BT-based Materials	42
CHAPTER 3 : METHODOLOGY		44
3.1	Introduction	44
3.2	The Samples Preparation Process	44
3.3	Samples Characterisation	47
3.3.1	X-Ray Diffraction Analysis	47
3.3.2	Impedance Spectroscopy Analysis	49
3.3.3	Piezoelectric Test Analysis	51
3.3.4	Scanning Electron Microscopic	53
CHAPTER 4 : RESULTS & DISCUSSION		55

4.1	Introduction	55
4.2	The ternary triangle diagram of BaTiO ₃ -BaSnO ₃ -BaZrO ₃	56
4.2.1	Structural analysis of the ternary diagram of BaTiO ₃ -BaSnO ₃ -BaZrO ₃	56
4.2.2	The dielectric properties of ternary diagram of BaTiO ₃ -BaSnO ₃ -BaZrO ₃	60
4.2.3	The Anomalous Dielectric Behaviour of BaSnO ₃	66
4.2.4	Summary	81
4.3	Oxygen Non-stoichiometry Effect on (Ba _{0.85} Ca _{0.15})(Zr _{0.10} Ti _{0.90})O ₃ (BCZT)	82
4.3.1	XRD Analysis on BCZT	83
4.3.2	The Impedance Spectroscopy Analysis of BCZT	86
4.3.3	The SEM Analysis of BCZT	102
4.3.4	Summary	103
4.4	The Novel Compositions of Sn-doped BCZT	104
4.4.1	The Structural Analysis of BCSZT System	104
4.4.2	Impedance Spectroscopy Analysis of BCSZT System	108
4.4.3	The Piezoelectric Properties of BCSZT System	115
4.4.4	The SEM Analysis of BCSZT System	117
4.4.5	The Effect of Sintering Temperature on BCSZT System	120
4.4.6	Summary	126
	CHAPTER 5 : CONCLUSIONS AND FUTURE OUTLOOK	127
5.1	Conclusions	127
5.2	Future Outlook	132
	REFERENCES	133
	LIST OF PUBLICATIONS	146

LIST OF TABLES

		PAGE
Table 2.1	Capacitance values and their possible interpretations (Sinclair, 1995).	18
Table 2.2	The list of piezoelectric properties (d_{33} and g_{33}), dielectric constant and their output power for typical piezoelectric materials.	23
Table 2.3	The summary of BT-based piezoelectric material properties.	43
Table 3.1	List of the raw materials drying temperatures and their product details.	45
Table 4.1	The lattice parameters of the BT, BS, BZ, BST50, BSZ50 and BZT50 obtained by least square refinement of the XRD data.	59
Table 4.2	The dielectric constant comparison between the BT, PZT and other lead-free materials which are commonly used in energy harvester applications.	62
Table 4.3	Curie-Weiss and Quadratic Law parameters for BCZT _{air} and BCZT _{N2} .	98
Table 4.4	Lattice parameters and tetragonality of BCSZT ceramics.	107
Table 4.5	The Curie-Weiss Law and Quadratic Law parameters, dielectric properties (T_c , ϵ_{max} , ϵ_r), piezoelectric constant (d_{33}), tolerance factor (t) and diffusiveness coefficient (γ).	112
Table 4.6	The piezoelectric constant, d_{33} values for a BCSZT system.	115
Table 4.7	The relative density comparison for BCSZT ceramics with different sintering temperatures.	120

Table 4.8 The piezoelectric energy harvester characteristics of BCSZT ceramics.

125

©This item is protected by original copyright

LIST OF FIGURES

	PAGE
Figure 1.1 Roadmap of energy harvesting rectification strategies (Cain & Mitcheson, 2012).	2
Figure 1.2 Direct and converse piezoelectric effects.	3
Figure 1.3 The schematic diagram of a piezoelectric material with its polarization and mechanical stress axis (Moheimani & Fleming, 2006).	5
Figure 1.4 The illustration of 33 mode and 31 mode operation for piezoelectric material (Roundy, Wright & Rabaey, 2003).	5
Figure 1.5 A ternary triangle diagram of BaTiO ₃ -BaSnO ₃ -BaZrO ₃ . The compositions being studied are shown by the black closed boxes.	10
Figure 2.1 The subclasses of a functional dielectrics.	15
Figure 2.2 The complex impedance plane format, Z'' vs Z' with their RC elements.	20
Figure 2.3 Piezoelectric timeline.	22
Figure 2.4 A perovskite structure.	24
Figure 2.5 A perovskite can be (a) non-centrosymmetric unit cell or distorted and becomes (b) centrosymmetric unit cell.	25
Figure 2.6 The distortion condition of a TiO ₆ octahedron in the perovskite structure of a tetragonal BaTiO ₃ (West, Adams, Morrison & Sinclair, 2004).	25
Figure 2.7 The polymorphism of barium titanate (Pan & Randall, 2010).	27

Figure 2.8	The phase diagram of BZT with $0.00 \leq x \leq 1.00$ based on the dielectric constant measurements (composition vs. temperature) (Maiti, Guo & Bhalla, 2011).	30
Figure 2.9	Phase transition of BZT based on dielectric permittivity measured at 1 kHz (composition vs. temperature).	31
Figure 2.10	The BZT phase structure by XRD patterns and Rietveld refinements.	33
Figure 2.11	Phase diagram of BST based on the dielectric measurements (Wei & Yao, 2007).	34
Figure 2.12	The XRD patterns of BSZT ceramics at 2θ of (a) 20° to 60° , (b) 44° to 46° , (c) 82.5° to 84° and (d) their Rietveld refinement assuming model of Amm2 and P4mm (Wang, Zhang, Ma, Zhao & Pei, 2017).	36
Figure 2.13	The triangle ternary diagram of a BaTiO_3 - BaSnO_3 - BaZrO_3 which shows the previous works being done including works from this research.	43
Figure 3.1	The methodology flow chart.	45
Figure 3.2	Sample preparation steps which consist of (a) weighing the raw material powders, (b) mixing and grinding the powders, (c,d,e) pelletizing the ground powders and (f) heating the pellets in a high-temperature box furnace.	46
Figure 3.3	The Bragg's law derivation (West, 2014).	48
Figure 3.4	The X-ray diffraction experiment (West, 2014).	49
Figure 3.5	A standard disk pellet diameter and thickness for all the samples prepared for the impedance measurement.	50
Figure 3.6	The impedance spectroscopy analysis setup which consists of a computer, a tube furnace and an impedance analyser.	51

Figure 3.7	A poling equipment setup.	52
Figure 3.8	A piezoelectric d_{33} meter measurement setup which consists of a shaker with probes to hold the sample.	53
Figure 3.9	A Quorum sputtering machine.	54
Figure 3.10	A ceramic microstructure analysis setup.	54
Figure 4.1	XRD patterns of (a) BaTiO ₃ (BT), (b) BaZrO ₃ (BZ) and (c) BaSnO ₃ (BS) which match the ICDD database.	57
Figure 4.2	(a) XRD patterns of BT, BS, BZ, BST50, BZT50, and BSZ50 with (b) enlarge peak (200) at 2θ between 42.5° to 47.5°.	58
Figure 4.3	(a) The lattice parameters and (b) unit cell volume obtained by using least square refinement of XRD data for BT, BS, BZ, BST50, BSZ50 and BZT50.	60
Figure 4.4	Dielectric constant vs. temperature for BaTiO ₃ measured at 1 kHz.	62
Figure 4.5	The dielectric constant vs. temperature for the BT, BS, BZ, BST50, BZT50 and BSZ50 measured at 1 kHz.	63
Figure 4.6	The dielectric loss vs. temperature for the BT, BS, BZ, BST50, BZT50 and BSZ50 measured at 1 kHz.	64
Figure 4.7	(a) The conductivity vs. temperature for the BT, BS, BZ, BST50, BZT50 and BSZ50 measured at 1 kHz and (b) the conductivities of various classes of materials.	65
Figure 4.8	Nyquist plots, Z'' versus Z' for BaSnO ₃ , measured at (a) 30 °C, (b) 60 °C, (c) 80 °C, (d) 100 °C, (e) 120 °C (f) 140 °C, (g) 160 °C, (h) 180 °C, (i) 200 °C, (j) 220 °C, (k) 240 °C, (l) 260 °C (m) 280 °C and (n) 300 °C.	67
Figure 4.9	Variations in Z' as a function of frequency at different temperatures.	69

Figure 4.10	Temperature dependence of the dielectric constant for BaSnO ₃ in (a) linear scale and (b) log scale.	71
Figure 4.11	The Z'' / M'' spectroscopy plot for BaSnO ₃ at 160 °C.	72
Figure 4.12	Variations of resistance of BaSnO ₃ as a function of frequency at different temperatures.	73
Figure 4.13	Variations of capacitance of BaSnO ₃ as a function of frequency at different temperatures.	74
Figure 4.14	The electrical conductivity of BaSnO ₃ as a function of frequency at different temperatures.	75
Figure 4.15	Electron hopping between a pair of adjacent Sn atoms.	79
Figure 4.16	An Arrhenius plot for the BaSnO ₃ temperatures between 30 °C to 300 °C.	80
Figure 4.17	(a) The comparison of XRD patterns between the BCZT _{air} and BCZT _{N₂} and the enlarged XRD patterns for (b) BCZT _{N₂} and (c) BCZT _{air} .	84
Figure 4.18	(a) Lattice parameters a and c and (b) unit cell volume of Ba _{0.85} Ca _{0.15} Zr _{0.10} Ti _{0.90} O ₃ with different processing conditions.	85
Figure 4.19	The Nyquist plots, Z'' versus Z' with fitted data by using (a) an equivalent circuit consisting of two sets of RC elements for the BCZT _{air} data measured at (b) 30 °C, (c) 90 °C, (d) 150 °C and (e) 200 °C.	88
Figure 4.20	The fitted capacitance versus frequency for the BCZT _{air} measured at (a) 30 °C, (b) 90 °C, (c) 150 °C and (d) 200 °C.	89
Figure 4.21	The capacitance vs. frequency for (a) BCZT _{air} and (b) BCZT _{N₂} .	90
Figure 4.22	The Z'' / M'' spectroscopy at 200 °C for BCZT _{air} .	91

Figure 4.23	The dielectric constant for (a) BCZT _{air} and (b) BCZT _{N₂} measured in a frequency range between 10 Hz to 100 kHz.	92
Figure 4.24	A comparison of dielectric constant between BCZT _{air} and BCZT _{N₂} measured at 1 kHz.	94
Figure 4.25	Measured density and relative density of BCZT _{air} and BCZT _{N₂} at the same temperature of 1400 °C.	96
Figure 4.26	The inverse dielectric constant at 1 kHz for (a) BCZT _{air} and (b) BCZT _{N₂} as a function of temperature.	97
Figure 4.27	The $\ln(1/\epsilon_r - 1/\epsilon_m)$ versus $\ln(T-T_m)$ at 1 kHz for (a) BCZT _{air} and (b) BCZT _{N₂} .	99
Figure 4.28	The dielectric loss of BCZT _{air} and BCZT _{N₂} versus temperature measured at 1 kHz.	100
Figure 4.29	The activation energy, E_a plot for BCZT _{air} .	101
Figure 4.30	The SEM micrographs of the BCZT _{air} ceramic (a-b) and BCZT _{N₂} ceramic (c-d).	103
Figure 4.31	(a) The XRD patterns of $(\text{Ba}_{0.85}\text{Ca}_{0.15})(\text{Sn}_x\text{Zr}_{x-0.10}\text{Ti}_{0.90})\text{O}_3$ ($0 \leq x \leq 0.1$) powders at 2θ from 20° to 80° , (b) the enlarged XRD patterns in 2θ range 44.8° - 47° .	105
Figure 4.32	(a) Lattice parameters a , and c of BCSZT and its (b) unit cell volume as a function of Sn content.	107
Figure 4.33	Nyquist plot for $(\text{Ba}_{0.85}\text{Ca}_{0.15})(\text{Sn}_x\text{Zr}_{x-0.10}\text{Ti}_{0.90})\text{O}_3$ ($0 \leq x \leq 0.1$) measured at 200 °C.	108
Figure 4.34	The electric modulus plane complex plot measured at 200 °C for $(\text{Ba}_{0.85}\text{Ca}_{0.15})(\text{Sn}_x\text{Zr}_{x-0.10}\text{Ti}_{0.90})\text{O}_3$ ($0 \leq x \leq 0.1$).	109
Figure 4.35	The dielectric constant for $(\text{Ba}_{0.85}\text{Ca}_{0.15})(\text{Sn}_x\text{Zr}_{x-0.10}\text{Ti}_{0.90})\text{O}_3$ ($0 \leq x \leq 0.1$) measured at 1 kHz with temperature range from 30 °C to 200 °C.	110

- Figure 4.36 The inverse dielectric constant as a function of temperature at 1 kHz for $(\text{Ba}_{0.85}\text{Ca}_{0.15})(\text{Sn}_x\text{Zr}_{x-0.10}\text{Ti}_{0.90})\text{O}_3$ ($0 \leq x \leq 0.1$). 112
- Figure 4.37 The $\ln(1/\varepsilon_r - 1/\varepsilon_m)$ versus $\ln(T - T_m)$ for $(\text{Ba}_{0.85}\text{Ca}_{0.15})(\text{Sn}_x\text{Zr}_{x-0.10}\text{Ti}_{0.90})\text{O}_3$ ($0 \leq x \leq 0.1$) measured at 1 kHz. 113
- Figure 4.38 Arrhenius plots of conductivity versus temperature of $(\text{Ba}_{0.85}\text{Ca}_{0.15})(\text{Sn}_x\text{Zr}_{x-0.10}\text{Ti}_{0.90})\text{O}_3$ ($0 \leq x \leq 0.1$) to obtain the activation energy, E_a at temperature from 170 °C to 200 °C. 116
- Figure 4.39 SEM micrographs of the surface of BCSZT ceramics with its histogram of grain size variations and EDX spectra. 119
- Figure 4.40 The comparison of dielectric constant for BCSZT ceramics at (a) $x = 0$, (b) $x = 0.025$, (c) $x = 0.050$, (d) $x = 0.075$ and (e) $x = 0.1$ between sintered at 1250 °C, 1350 °C and 1450 °C. 121

LIST OF ABBREVIATIONS

BME	Base Metal Electrode
BS	Barium Stannate
BT	Barium Titanate
BZ	Barium Zirconate
BST	Barium Stannate Titanate
BSZ	Barium Stannate Zirconate
BZT	Barium Zirconate Titanate
BCST	Barium Calcium Stannate Titanate
BCZT	Barium Calcium Zirconate Titanate
BSZT	Barium Stannate Zirconate Titanate
BCSZT	Barium Calcium Stannate Zirconate Titanate
CPE	Constant Phase Element
DPT	Diffuse Phase Transition
EDX	Energy Dispersive X-ray
EIA	Electrical Industry Alliance
EU	European Union
FE	Ferroelectric
FoM	Figure of Merit
ICDD	International Center for Diffraction Data
MLCA	Multilayer Ceramic Actuator
MLCC	Multilayer Ceramic Capacitor
MPB	Morphotropic Phase Boundary
PDF	Powder Diffraction File
PE	Paraelectric
PVDF	Poly (Vinylidene fluoride)
PZT	Plumbum Zirconate Titanate
SEM	Scanning Electron Microscopy
TEM	Transmission Electron Microscopy
XRD	X-ray Diffraction

LIST OF SYMBOLS

a	Lattice a
A	Electrode area
c	Lattice c
c	Lattice c
C	Capacitance
C_0	Vacuum capacitance
$^{\circ}\text{C}$	Degree celcius
d	Interplanar spacing
d_{33}	Piezoelectric constant
D	Dielectric displacement
eV	Electron volt
E	Applied electric field
E_a	Activation energy
f	Frequency
F	Farad
g_{33}	Piezoelectric voltage constant
K_b	Boltzmann's Constant
l	Electrode separation
M^*	Complex electric modulus
P	Output power
Q	Charge
r_A	Ionic radii of A -site cation
r_B	Ionic radii of B -site cation
r_O	Ionic radii of oxygen anion
R	Resistance
S	Strain
t	Tolerance factor
$\tan \delta$	Dielectric loss
T	Applied stress
T_c	Curie temperature
T_{cw}	Curie-Weiss constant
ΔT	Deviation from the Curie-Weiss law
Y^*	Complex admittance
Z'	Real part of Impedance
Z''	Imaginary part of Impedance

Z^*	Complex impedance
ϵ_0	Dielectric constant in vacuum
ϵ_r	Relative dielectric constant
ϵ'	Real part of dielectric constant
ϵ''	Imaginary part of dielectric constant
ϵ^*	Complex dielectric constant
σ	Conductivity
σ_{ac}	AC conductivity
σ_0	Pre-exponential term
θ	Diffraction angle
γ	Diffuseness coefficient
λ	Wavelength of X-rays
ρ	Resistivity
ω	Angular frequency

©This item is protected by original copyright

Sintesis dan Pencirian Bahan Pizoelektrik Berasaskan BaTiO₃ Untuk Aplikasi Penuaian Kuasa

ABSTRAK

Kesedaran tentang bahayanya penggunaan plumbum terhadap alam sekitar telah menjurus kepada pembuatan bahan piezoelektrik bebas plumbum dan menjadi bahan alternative kepada plumbum zirkonat titanat (PZT) yang telah mendominasi pasaran piezoelektrik pada masa kini. Bahan-bahan berasaskan barium titanat (BT) adalah antara bahan piezoelektrik bebas plumbum. Oleh itu, projek ini melibatkan kesan penggantian Sn, Zr dan Ca dalam BT bagi meningkatkan prestasi dielektrik dan piezoelektriknya. Kesan oksigen bukan stoikiometri dan kondisi sinter juga telah dilakukan. Kesemua sampel disediakan melalui kaedah sintesis keadaan pepejal konvensional pada suhu antara 1250-1450 °C dalam udara selama 3 jam. Pencirian kesemua sampel telah dilakukan dengan menggunakan Pembelauan sinar-X (XRD), Analisis Impedans Spektroskopi (diukur pada suhu 30-200 °C, antara 10-100 kHz), Ujian piezoelektrik (dikutubkan pada 30 °C, 4.5 kV/mm selama 30 mins) dan Mikroskop Imbasan Elektron (SEM). Projek ini melibatkan tiga kajian utama. Dalam kajian pertama, analisis struktur dan dielektrik bagi rajah segitiga BaTiO₃ (BT) - BaSnO₃ (BS) - BaZrO₃ (BZ) telah dilakukan. Kesan penggantian Zr dan Sn pada bahagian Ti telah dikaji. BT, BS, BZ, BaSn_{0.5}Ti_{0.5}O₃ (BST50), BaZr_{0.5}Ti_{0.5}O₃ (BZT50) and BaSn_{0.5}Zr_{0.5}O₃ (BSZ50) telah disediakan dan kesemuanya telah mencapai fasa tulen. Dalam kajian ini, BS telah memperoleh ciri dielektrik anomali yang sangat tinggi dengan nilai konstant dielektrik, ϵ_r sebanyak 87,290 diukur pada 10 Hz dan 6027 pada 1 kHz dimana ianya disebabkan oleh kesan pasangan tunggal dari Sn akibat daripada oksigen bukan stoikiometri oleh BS. Kajian kedua adalah berkenaan sistem Ba_{0.85}Ca_{0.15}Zr_{0.10}Ti_{0.90}O₃ (BCZT) setelah ia dilaporkan mempunyai nilai piezoelektrik konstant yang tinggi. Kebaharuan dalam kajian ini adalah pemerhatian kesan oksigen bukan stoikiometri terhadap ciri dielektriknya. Nilai ϵ_r bagi BCZT_{air} (dipanaskan dalam udara) sebanyak 4805 adalah lebih tinggi berbanding BCZT_{N₂} (dipanaskan dalam gas N₂) iaitu 4771. Nilai ϵ_r bagi BCZT_{N₂} tidak menunjukkan perubahan ketara disebabkan oleh struktur BCZT yang telah stabil. Kajian ketiga pula tentang kesan penggantian Sn dalam sistem BCZT. Seramik (Ba_{0.85}Ca_{0.15})(Sn_{*x*}Zr_{0.10-x}Ti_{0.90})O₃, BCSZT (*x* = 0, 0.025, 0.05, 0.075, 0.1) disediakan dan kesemuanya mencapai fasa tulen dengan struktur tetragonal. Nilai ϵ_r meningkat apabila kandungan Sn meningkat dan T_c pula menurun dari 95 °C ke 59 °C. T_c beralih ke suhu lebih rendah disebabkan radii ionik Sn⁴⁺ yang lebih kecil telah menggantikan Zr⁴⁺ pada kawasan-B. Ia telah mengecilkan ikatan Ti-O lalu melemahkan interaksi dalam oktahedral TiO₆. Faktor toleransi yang lebih besar memudahkan lencongan Sn⁴⁺ pada kawasan-B dalam struktur oktahedral lalu meningkatkan ciri ferroelektrisiti dan dielektriknya. Namun, ciri piezoelektriknya menurun apabila tetragonaliti sampel menurun. Paksi *c* menjadi lebih pendek dan mengurangkan momen dwikutub oktahedral TiO₆. BCSZT pada *x* = 0.025 adalah komposisi baru dengan ciri-ciri piezoelektrik tertinggi dan sesuai bagi aplikasi penuain kuasa piezoelektrik. Ia memperoleh nilai konstant piezoelektrik, d_{33} sebanyak 213 pC/N apabila tersinter pada suhu 1350 °C dan kuasa keluaran, *P* sebanyak 18.2x10⁻³ Vm/N dan konstant voltan piezoelektrik, g_{33} sebanyak 3.51 pm³/J tersinter pada 1250 °C.

Synthesis and Characterisation of BaTiO₃-based Piezoelectric Materials for Energy Harvester Applications

ABSTRACT

There has been renewed interest in developing lead-free piezoelectric materials as the alternative to the toxicity of lead zirconate titanate (PZT) which currently dominates the market of piezoelectric materials. Some of the promising lead-free piezoelectric materials are those based on barium titanate (BT). This project is embarked to study the doping effects of Sn, Zr and Ca into a BT-based piezoelectric material to enhance its piezoelectric and dielectric properties. The effects of oxygen non-stoichiometry and sintering conditions in improving the performance of the piezoelectric materials are also studied. All the samples were synthesized by a conventional solid state route at temperatures between 1250-1450 °C in air for 3 hours. The samples were characterised by using X-ray Diffraction (XRD), Impedance Spectroscopy Analyser (measured at 30-200 °C, between 10-100 kHz), piezoelectric test (poled at 30 °C, 4.5 kV/mm for 30 mins) and Scanning Electron Microscope (SEM). This project involves three main investigations. Firstly, a structural study and dielectric analysis of a ternary triangle diagram of BaTiO₃ (BT)-BaSnO₃ (BS)-BaZrO₃ (BZ) were carried out. The doping effects of Zr and Sn at the Ti-site were investigated. The BT, BS, BZ, BaSn_{0.5}Ti_{0.5}O₃ (BST50), BaZr_{0.5}Ti_{0.5}O₃ (BZT50) and BaSn_{0.5}Zr_{0.5}O₃ (BSZ50) were prepared and all the samples are of a single phase. In this study, the BS has shown a giant anomalous dielectric behaviour with dielectric constants, ϵ_r of about 87,290 and 6027 measured at 10 Hz and 1 kHz, respectively, which are contributed by the lone pair effect of the Sn due to the oxygen non-stoichiometry of the BS. Secondly, the Ba_{0.85}Ca_{0.15}Zr_{0.10}Ti_{0.90}O₃ (BCZT) system was investigated as it was reported to exhibit a high piezoelectric constant, d_{33} value. The novelty in this second investigation is the observation of the effects of the oxygen non-stoichiometry in the BCZT composition toward its dielectric properties. The ϵ_r value of the BCZT_{air} (sintered in air) is slightly higher than the BCZT_{N₂} (sintered in N₂) of $\epsilon_r = 4805$ and 4771, respectively. The dielectric constant of the BCZT_{N₂} does not show much differences due to the fact that the BCZT structure is already stable. The third investigation was to study the effects of Sn substitution in the BCZT system. The (Ba_{0.85}Ca_{0.15})(Sn_{*x*}Zr_{0.10-*x*}Ti_{0.90})O₃, BCSZT ($x = 0, 0.025, 0.05, 0.075, 0.1$) ceramics were prepared. All the samples are of a single phase and exhibit a tetragonal structure. The ϵ_r value increases as the Sn content is increased and the T_c is lowered from 95 °C to 59 °C. The T_c shifts to a low temperature as the Sn⁴⁺ with smaller ionic radii replaces the Zr⁴⁺ at the B-sites. It decreases the Ti-O bonds thus weakening the interactions within the TiO₆ octahedral. The larger tolerance factor eases the deviation of the Sn⁴⁺ ion at the B-sites in the octahedral structure and enhances its ferroelectricity and dielectric properties. However, the d_{33} value decreases since the tetragonality of the samples decrease. The *c*-axis becomes shorter and reduces the dipole moment of the TiO₆ octahedral. The BCSZT at $x = 0.025$ is found out to be the novel composition with the highest piezoelectric properties, and is suitable for piezoelectric energy harvester applications. It obtains the highest $d_{33} = 213$ pC/N when sintered at 1350 °C and the highest piezoelectric voltage constant, g_{33} and output power, P when sintered at 1250 °C of about 18.2×10^{-3} Vm/N and 3.51 pm³/J, respectively.

CHAPTER 1 : INTRODUCTION

1.1 Background

Piezoelectric has been used in several applications such as actuators, flexible electronics, resonators, medical sensors, tactile sensors, and energy harvesting. The usage of piezoelectric materials in energy harvester applications is one of the current trends nowadays. Piezoelectric has been installed on several freeways and flooring in California and London to harvest electrical energy (Dagdeviren et al., 2016; Goldman, 2016; Guo & Lu, 2017). Piezoelectric energy harvester has become one of the best options of energy harvester transducer in the electronic industry. It can convert mechanical energy to electrical energy directly and requires less area which makes it easy to assemble as compared to other energy harvesters such as solar panel, electrostatic and electromagnetic energy harvesting applications (Wang & Wu, 2012).

Several research on energy harvester applications have been investigated to enhance the energy harvester applications' performance efficiency. In 2012, Cain and Mitcheson have concluded the energy harvesting research areas that are likely to receive the most attention in the near future as illustrated in Figure 1.1 (Cain & Mitcheson, 2012). Each research area has its own targets, assurance of deliverables, technologies and the enabler in science. The roadmap has also foreseen that from 2018 onwards, the research area that will be of interest to the researchers would be on the system integration and development of new materials. Thus, finding and developing new piezoelectric materials with high piezoelectric properties have become the aim of this research.

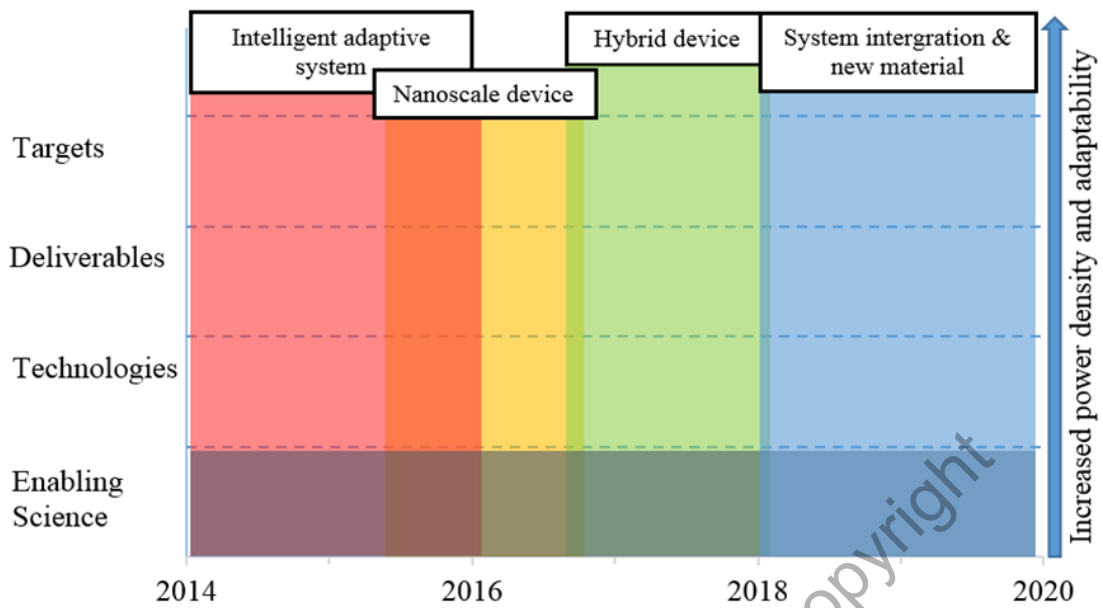


Figure 1.1 Roadmap of energy harvesting rectification strategies (Cain & Mitcheson, 2012).

1.1.1 Piezoelectric Operation Concept

Piezoelectricity was discovered by Jacques and Pierre Curie back in 1880 (Jaffe, 1971). Piezoelectric material must be polarized to align all the dipoles in the same direction to achieve maximum piezoelectric properties. The piezoelectric materials must exhibit both direct and converse effects. The polarized piezoelectric material can develop electrical charges due to the mechanical stress applied and is known as a direct piezoelectric effect. These materials should also show the converse phenomenon, where a geometric strain can be developed by an applied voltage, which is known as the converse piezoelectric effect. Figure 1.2 shows the direct and converse piezoelectric effects.

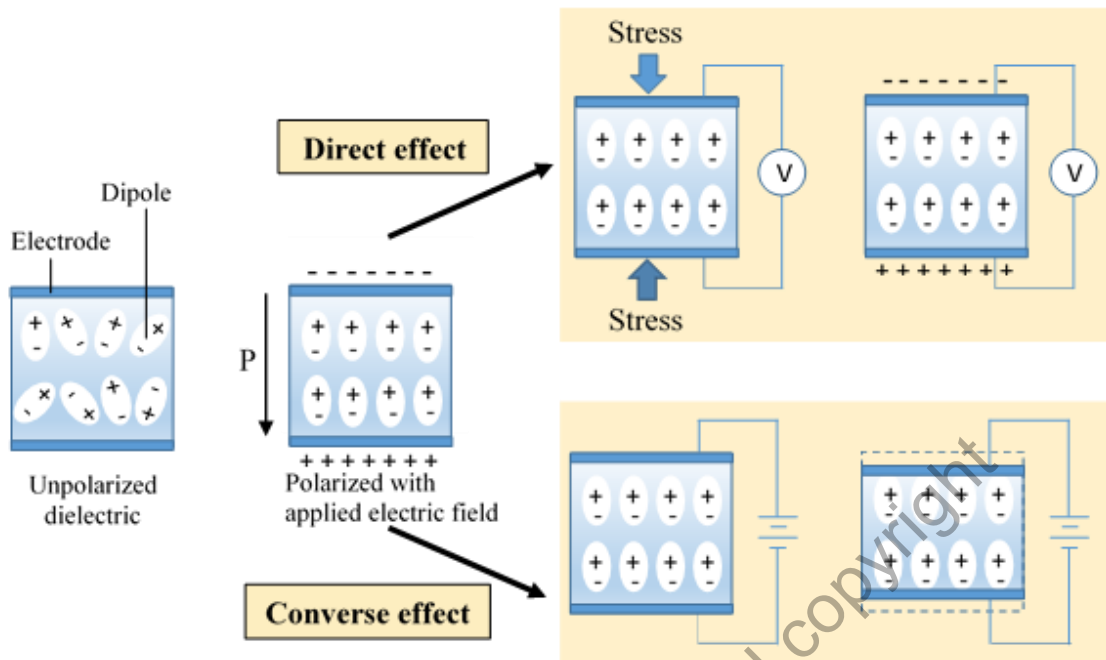


Figure 1.2 Direct and converse piezoelectric effects.

All materials that exhibit piezoelectricity have a crystallographic requirement in which the materials must have non-centrosymmetric unit cells (Aksel & Jones, 2010). The piezoelectric material unit cells consist of dipoles with random directions. Dipole refers to a separate concentration between the negative and positive electric charges. Normally, these dipoles cancel each other out and there is no net separation of charge in the unit cells. Polarization is needed for piezoelectric material to induce interaction between the dipoles. The polarization process allows the dipoles of the material to be aligned with the same direction when there is an applied electric field, thus enhancing the piezoelectricity. Once stress is applied to the piezoelectric materials, the atoms shift, resulting in an asymmetrical and charge distribution within the unit cells. Therefore, the dipoles have a net separation of positive and negative charges due to the applied stress and produced voltage. When an electric field is applied to the material, it induces a geometric strain which is also known as the converse effect.

1.1.2 Figure of Merits of Piezoelectric Materials in Energy Harvesters

There are several figure of merits (FoMs) which have been applied to evaluate the energy conversion efficiency of the piezoelectric energy harvester applications. The most common FoMs that are widely used for piezoelectric material involve the piezoelectric charge constant, d_{ij} (unit, pC/N or pm/V) and piezoelectric voltage constant, g_{ij} (unit, m²/C or mV/N). High d_{ij} value represents the ability of the material to develop motion or vibration while high g_{ij} value indicates that the material has high desirability to generate a voltage from a mechanical stress. The FoMs for the piezoelectric materials selected for energy harvester applications require high d_{ij} and g_{ij} values (Xu & Kim, 2012; Xiong & Wang, 2016; Todaro et al., 2017; Uchino & Ishii, 2010). The product value of d_{ij} and g_{ij} indicates the output electric power, P as shown in Equation 1.1:

$$P \propto g_{ij} \cdot d_{ij} \quad (1.1)$$

1.1.3 Polarization Direction and Mechanical Stress Axis Nomenclature

The piezoelectric properties can be determined based on the polarization direction and the mechanical stress axis applied to the piezoelectric material. These axes are represented by subscript i and j alongside the piezoelectric properties symbols (piezoelectric charge constant, d_{ij} and piezoelectric voltage constant, g_{ij}). The axis nomenclature is demonstrated in Figure 1.3. The subscript i denotes the axes numbered 1, 2 and 3 which is similar to the Cartesian coordinate axes x , y , and z respectively. It represents the polarization direction. Although subscript j denotes the same three axes,

but it is numbered from 1 to 6 to define the directions of the mechanical stress or strain and also the shear stress or strain in rotational motions around them (number 4, 5 and 6 indicate shear around x , y , and z respectively) (Toprak & Tigli, 2014). Typically, axis 3 is assigned as the direction of the polarization of the piezoelectric material. When the mechanical stress applied is in the same direction as the polarization axis 3, it indicates that the piezoelectric material is operated in a 33-mode (d_{33} and g_{33}). Under a 31-mode, the material is poled in the direction of 3 and the mechanical stress acts in the direction of 1 (d_{31} and g_{31}) as depicted in Figure 1.4.

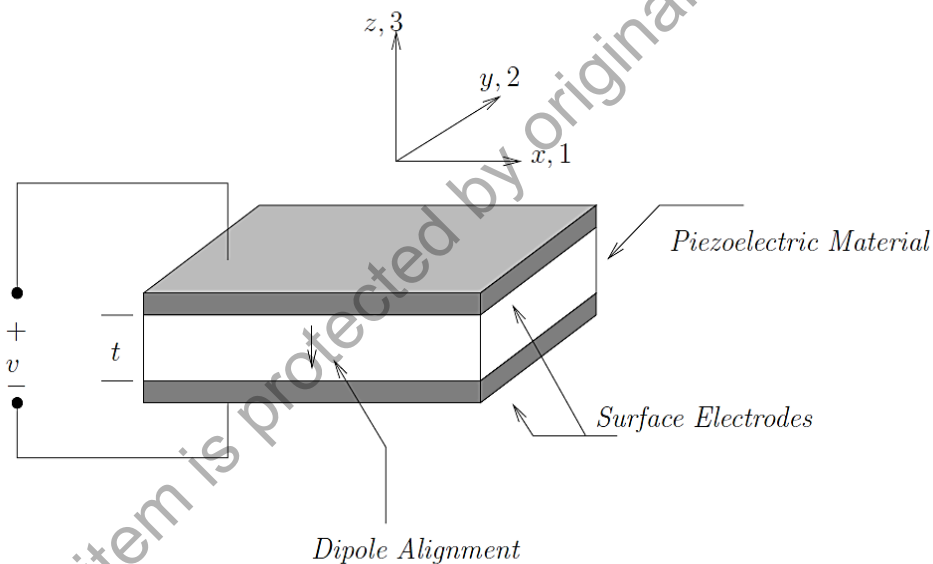


Figure 1.3 The schematic diagram of a piezoelectric material with its polarization and mechanical stress axis (Moheimani & Fleming, 2006).

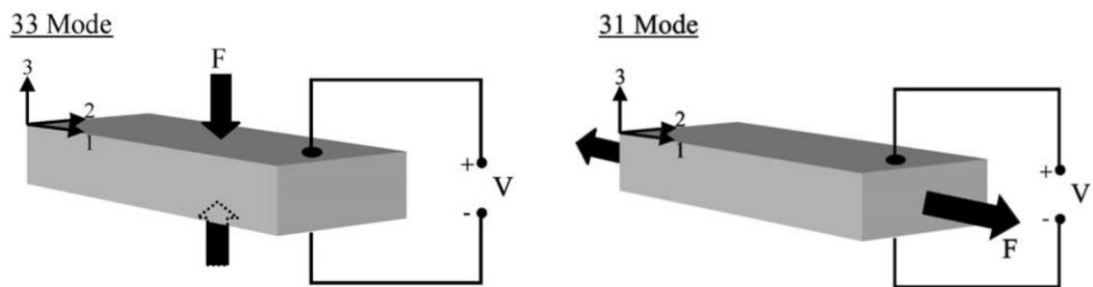


Figure 1.4 The illustration of 33 mode and 31 mode operation for piezoelectric material (Roundy, Wright & Rabaey, 2003).

Operation in a 31-mode can be applied to flexible thin elements in which a large strain is developed in the direction of 1 through the bending of the elements (e.g. piezoelectric bimorphs) (Roundy, Wright & Rabaey, 2003). Baker et al., 2005 have compared the energy harvesters' productivity between piezoelectric materials operated under the 31-mode and 33-mode and concluded that the piezoelectric material under the 31-mode is more efficient to convert lower-level loads/force/deformation into electrical energy. However, when the piezoelectric material is under a higher-level load such as the piezoelectric material installed under the pavement with high load induced by vehicle movements, the conversion is more efficient under the 33-mode (Baker, Roundy & Wright, 2005). The energy harvester under the 33-mode show that the energy productivity increases linearly with the stress applied along the direction of the poled material (Xiong & Wang, 2016). Piezoelectric material operated under the 33-mode is studied most extensively (Zhang, Glaum, Groh, Ehmke, Blendell, Bowman et al., 2014; Khandelwal, Gupta, Laishram & Singh, 2019; Baraskar, Kadhane, Darvade, James & Kambale, 2018; Wang, Liu, Liang & Yang, 2018; Zhou, Liu, Xu, Yao & Cai, 2017; Zhang, Sun & Chen 2018). In this research, all the samples involved with the 33-mode.

Another comparison was done by Ramsay and Clark in 2001, which concludes that the 31-mode conversion may benefit the energy conversion of a piezoelectric material under very low pressure sources, while the 33-mode may be feasible for piezoelectric material with greater volume (Ramsay & Clark, 2001). The piezoelectric material can achieve higher output energy in the 33-mode conversion by increasing the piezoelectric material layers by stack configurations while the 31-mode stress might be easily achieved by bonding the piezoelectric element to a substructure in which they undergo bending and stretch together (Roundy, Wright & Rabaey, 2003).